

Lagrangian investigation of the precipitation efficiency of convective clouds

Wolfgang Langhans*

Earth Sciences Division, Lawrence Berkeley National Laboratory, Berkeley, California, USA

Kyongmin Yeo

IBM T.J. Watson Research Center, Yorktown Heights, New York, USA

David M. Romps

*Dept. of Earth and Planetary Science, University of California, Berkeley
Earth Sciences Division, Lawrence Berkeley National Laboratory, Berkeley, California, USA*

**Corresponding author address:* Wolfgang Langhans, Mailstop 84R0171, Earth Sciences Division, Lawrence Berkeley National Laboratory, Berkeley, CA 94720.
E-mail: wlanghans@lbl.gov

ABSTRACT

The precipitation efficiency of cumulus-congestus clouds is investigated with a new Lagrangian particle framework for large-eddy simulations. The framework is designed to track particles representative of individual water molecules. A Monte-Carlo approach facilitates the transition of particles between the different water classes (e.g., vapor, rain, or graupel). With this framework, it is possible to reconstruct the pathways of water as it moves from vapor at a particular altitude to rain at the surface. By tracking water molecules through both physical and microphysical space, the precipitation efficiency can be studied in detail as a function of height.

Large-eddy simulations of individual cumulus-congestus clouds show that the clouds convert entrained vapor to surface precipitation with an efficiency of around 10%. About 2/3 of all the vapor that enters the cloud does so by entrainment in the free troposphere, but free-tropospheric vapor accounts for only 1/3 to 1/2 of the surface rainfall, with the remaining surface rainfall originating as vapor entrained through the cloud base. The smaller efficiency with which that laterally entrained water is converted into surface precipitation results from the smaller efficiencies with which it condenses, forms precipitating hydrometeors, and reaches the surface.

1. Introduction

A cloud's precipitation efficiency (PE) – loosely defined as the efficiency with which it converts vapor to surface precipitation – can have a large impact on the detrained cloud cover, cloud radiative forcing, and, through its impact on the profiles of radiative and latent heating, the large-scale atmospheric circulation. As a consequence, parameters related to precipitation efficiency in global climate models have a large influence on the simulated climate (Knight et al. 2007; Sanderson et al. 2008; Yang et al. 2012, 2013).

Previous studies reported a wide range of possible PEs partly as a result of different underlying definitions. Observational studies typically defined PE as the precipitating fraction of the vapor mass fluxed into a cloud (Braham 1952; Auer and Marwitz 1968; Fankhauser 1988). Analogously, drying ratios (DR) have been used to quantify the amount of water extracted by surface rainfall from the atmosphere in flows over mountains (Smith et al. 2003; Kirshbaum and Smith 2008). In numerical experiments, PE was commonly defined as the ratio of precipitation rates over condensation rates (Murray and Koenig 1972; Weisman and Klemp 1982; Pauluis and Held 2002; Cohen and McCaul 2007; Romps 2011). Both of the aforementioned estimates were based on either instantaneous rates or time-integrated totals.

Unfortunately, such definitions may result in efficiencies larger than one (Auer and Marwitz 1968; Sui et al. 2005) since, e.g., in the case of a condensation PE, the release of stored hydrometeors and/or hydrometeor advection from remote regions are not taken into account as rainfall sources (Sui et al. 2007). This issue is inherently tied to the Lagrangian nature of water transformations. Irrespective of its evolution in physical space, once a water molecule is provided to a cloud (entrainment stage), it may eventually condense (condensation stage), become part of a falling hydrometeor (formation stage), and might even reach the surface (sedimentation stage). It is natural to define condensation, formation, and sedimentation efficiencies of cloud-processed water as the conditional probabilities of water molecules to reach certain stages in this cycle. As an example, the formation efficiency equals the average probability of water molecules to form precipitation given that they condensed before (in the particular cloud or storm system being studied).

Even though a different approach was pursued in their study, Lasher-Trapp et al. (2005) demonstrated the utility of Lagrangian investigations of microphysical processes in cumulus clouds. To measure the above listed efficiencies, a new framework is developed here to track representative water molecules within large-eddy simulations of moist convection. Previous studies have used Lagrangian particles to record the trajectories of dry air (e.g., Heus et al. 2008; Yeo and Romps 2013). We may think of those studies as using Lagrangian particles to track representative nitrogen molecules. Here, we use Lagrangian particles to track representative water molecules in a similar fashion. However, since water molecules can exist in different types of water classes (in this study, there are six classes corresponding to vapor, cloud liquid, cloud ice, rain, snow, and graupel), the molecules must be tracked through microphysical space as well as physical space. To accomplish this task, each Lagrangian particle must move through physical space (i.e., x , y , and z) and microphysical space (i.e., in which of the six classes it resides) in the same way as actual water molecules. Particles associated with a precipitating class must fall relative to the mean flow with the appropriate terminal velocity. Particles in a region of the cloud where molecules are being exchanged between water classes must hop from class to class with the same statistics, which is accomplished here with a stochastic Monte Carlo method. Note that this particle-molecule analogy is limited in realism by the underlying microphysical scheme. With the bulk scheme used here, it is not possible to account for the last-in/first-out mechanism that would apply to molecules that freeze onto a hailstone, and no accounting is made for the exchange of molecules between vapor and condensed phases that occurs in equilibrium.

The introduced framework allows for a straightforward definition of PE, namely as the fraction of condensed particles that subsequently rains out. Equivalently, PE may be viewed as the probability of a water molecule to reach the surface given that it condensed at least once earlier on. Analogously, a drying ratio DR is defined as the probability of a water molecule to reach the

surface given that it entrained into the cloud at least once. DR is related to PE as

$$DR = CE \cdot PE = CE \cdot FE \cdot SE, \quad (1)$$

where CE is the condensation efficiency and PE is the product of the formation efficiency FE and the sedimentation efficiency SE. CE, FE, and SE are defined as the conditional probabilities to reach the condensation, formation, and sedimentation stages, respectively, given that the previous stage in the cycle had been reached at least once.

In his early studies, Braham (1952) estimated the average DR and PE of observed precipitating thunderstorms to be as small as 10% and 19%, respectively. In more recent numerical studies, comparably small values of $\sim 20\%$ have been reported for PE (e.g., Pauluis and Held 2002; Roms 2011). It is unclear, however, what controls those small DRs and PEs. Since several studies report that undiluted air parcels are exceedingly rare (Zipser 2003; Kuang and Bretherton 2006; Roms and Kuang 2010), one hypothesis is that turbulent mixing reduces the in-cloud residence time of water considerably. This would render condensation efficiencies considerably smaller than those of adiabatic parcel ascents within protected cloud cores. As an example, one may think of two moles of water rising in a cloud with a high chance to condense. In a mixing event these two moles might get replaced by one mole from the environment of the cloud. The latter will end up in the cloud, but with a lower chance for condensation. Adding to this detrimental effect, the mixing process might also lower the buoyancy of air hosting other vapor molecules that rise inside the cloud.

The role of undiluted cloud cores for cumulus dynamics has been emphasised in other studies (Blyth et al. 2005; Damiani et al. 2006; Carpenter et al. 1998; Zhao and Austin 2005) and their existence is frequently explained by the theory of shedding thermals (Scorer and Ludlam 1953; Blyth et al. 1988). The latter concept describes rising bubbles that entrain and mix environmental air in their wakes, but retain an undiluted upper core. If the erosion rate of these cores is small enough, this could imply that vapor entrained through cloud base (and then residing in these cores) has on average longer in-cloud residence times than vapor entrained laterally and thus also a higher condensation efficiency.

This ultimately raises another question: how much water is contributed to surface precipitation from each height range in the atmosphere? The answer to this question has implications for cloud-seeding experiments (Auer and Marwitz 1968; Fankhauser 1988), aerosol-cloud interactions (e.g., Phillips et al. 2005; van den Heever et al. 2011), and, in particular, the scavenging of aerosols (Respondek et al. 1995). Also, the thermodynamic scaling of tropical extreme precipitation with surface temperature can be expected to depend on the respective fractions of precipitation originating from the lower and upper troposphere, simply, because in the tropics the water vapor content at the surface scales at a lower rate with surface temperature than the column-integrated water vapor content (O’Gorman and Muller 2010; Muller et al. 2011).

In this study, the Lagrangian framework described above is combined with large-eddy simulations (LES) of cumulus clouds. The original height of precipitating water vapor will be determined by quantifying the nonlocal transport of water by means of transilient matrices. For example, the matrix for entraining vapor will be obtained by binning all particles that entrain at least once according to their origin height and destination height. Based on this approach, the early picture of the transport and processing of water by cumulus clouds (e.g., Braham 1952) is updated and the efficiencies of cloud-base vapor (origin height below cloud base) and laterally entrained vapor (origin height above cloud base) are determined. Our motivation here is to apply the developed Lagrangian framework to gain new insights into cloud efficiencies from a few simulations.

The outline of the paper is as follows. The new Lagrangian framework is introduced in section 2 and its coupling to LES is explained in section 3. The transilient matrix for water and the resulting water budget of cumulus clouds are presented in section 4. The height and time dependence of cloud efficiencies are presented in section 5, and section 6 summarizes the conclusions.

2. Stochastic Lagrangian particle framework

a. General description

The Lagrangian particles used here are passive in the sense that their presence does not affect the Eulerian LES. The particles are simply diagnostic, recording a history of their position and microphysical state as they go. Each Lagrangian particle is assigned to one water class at a time, just as a water molecule resides in one water class at a time. Despite the focus here on water, this framework is generally applicable to the tracking of mass through any non-conserved (i.e., non-passive, or active) Eulerian categories. This could include the tracking of oxygen through different oxygenated compounds in a study of atmospheric chemistry, the tracking of carbon through different combustion products in a numerical simulation of an engine, or the tracking of baryons through various isotopes in a fission reaction. No matter the application, the goal is to capture the movement of mass through physical and microphysical (or chemical or nuclear) space in a statistical sense by tracking a large number of representative molecules, atoms, or baryons.

To accomplish this, the Lagrangian particles must move through physical and microphysical space in a way that conserves, in a statistical sense, the ratio of the number density of particles in category i to the mass density of Eulerian water in category i . We can state this mathematically if we denote the number of particles per volume in category i as N_i and the mass of Eulerian water per volume in category i as ρ_i . We wish to conserve, as closely as possible, the specific number density $N_i^* = N_i/\rho_i$ (kg^{-1}). Furthermore, we want each particle to represent the same amount of water mass, so the particles will be initialized in the simulation such that $N_i^*(x, y, z)$ has a homogeneous distribution in space and the same value for all i , i.e., $N_i^*(x, y, z)$ takes the same constant value for all x, y, z , and i . Given the category i of a particle, its position evolves in time as

$$\frac{d\mathbf{x}_i}{dt} = \mathbf{u}_i = \mathbf{u}_a + \mathbf{u}_{if}, \quad (2)$$

with $u_i^m = u_a^m + u_{if}^m$ the m -th component of the velocity vector, u_a^m the m -th component of the dry-air velocity vector, and u_{if}^m the velocity of mass in class i with respect to dry air. In the case of atmospheric water, $\mathbf{u}_{if} = (0 \ 0 \ u_{if})^T$ represents the free-fall speed of a precipitating water class.

For a compressible flow, the conservation equations for any non-conserved Eulerian mass density ρ_i (kg m^{-3}) and its corresponding particle number density N_i (m^{-3}) are given by

$$\frac{\partial \rho_i}{\partial t} = -\frac{\partial}{\partial x^m}(\rho_i u_i^m) + \dot{\rho}_i \quad (3)$$

$$\frac{\partial N_i}{\partial t} = -\frac{\partial}{\partial x^m}(N_i u_i^m) + \dot{N}_i \quad (4)$$

with $\dot{\rho}_i$ the net mass source and \dot{N}_i the net particle source due to conversion of mass between the categories. The mass sources $\dot{\rho}_i$ are parameterized within Eulerian frameworks and could represent sources due to, e.g., chemical reactions or microphysical transformations.

Combining (3) and (4) yields the conservation equation for N_i^* as

$$\rho_i \frac{\partial N_i^*}{\partial t} = -\rho_i u_i^m \frac{\partial N_i^*}{\partial x^m} + \left(\dot{N}_i - N_i \frac{\dot{\rho}_i}{\rho_i} \right). \quad (5)$$

Since N_i^* shall be homogenous in space (at least statistically), conservation of N_i^* is satisfied if

$$\frac{\dot{N}_i}{N_i} = \frac{\dot{\rho}_i}{\rho_i}, \quad (6)$$

i.e., if the fractional mass and number-density sources are equal. The net source of mass in a category may be decomposed further into individual rates $\dot{\rho}_{ij}$ from j to i , which are non-negative by definition. In terms of these individual rates, $\dot{\rho}_i$ is given by

$$\dot{\rho}_i = \sum_{j \neq i} \dot{\rho}_{ij} - \sum_{j \neq i} \dot{\rho}_{ji}. \quad (7)$$

Combining equations (6) and (7), and using the fact that $N_i^* = N_j^*$, we obtain

$$\dot{N}_i = \sum_{j \neq i} \frac{\dot{\rho}_{ij}}{\rho_j} N_j - \sum_{j \neq i} \frac{\dot{\rho}_{ji}}{\rho_i} N_i. \quad (8)$$

If this were integrated with an Euler scheme, N_i would be advanced by a time step δt according to

$$N_i(t + \delta t) = N_i(t) + \sum_{j \neq i} \frac{\delta t \dot{\rho}_{ij}}{\rho_j} N_j - \sum_{j \neq i} \frac{\delta t \dot{\rho}_{ji}}{\rho_i} N_i. \quad (9)$$

For a particular grid cell and time step of the LES, this equation tells us that the number of i particles that should be converted to j particles is $\delta t N_i \dot{\rho}_{ji} / \rho_i$. In this study of clouds, the $\dot{\rho}_{ji}$ comes from a microphysical parameterization, which knows nothing about the Lagrangian particles. Therefore, unless $\delta t N_i \dot{\rho}_{ji} / \rho_i$ is zero or one, it will not be an integer. This means that we must grapple with the following questions: which of the particles in category i should switch to category j , and how do we convert fractions of a particle?

b. Particle transitions

A stochastic framework is used here to address these questions. In this scheme, particles switch randomly between categories with transition probabilities prescribed such that Eq. (9) is satisfied on average. Equation (9) can be written in matrix form as

$$\mathbf{N}(t + \delta t) = \mathbf{P}(t) \mathbf{N}(t), \quad (10)$$

where the probability matrix \mathbf{P} is defined by

$$P_{ij} = \begin{cases} \delta t \dot{\rho}_{ij} / \rho_j & \text{for } i \neq j \text{ and } \rho_j > 0 \\ 1 - \sum_{k \neq i} \delta t \dot{\rho}_{ki} / \rho_i & \text{for } i = j \text{ and } \rho_j > 0 \\ 0 & \rho_j = 0 \end{cases}. \quad (11)$$

The diagonal elements of \mathbf{P} correspond to the probability of a particle staying in its own category, while off-diagonal elements describe the probability of switching from category j to category i . Note that \mathbf{P} can be interpreted as a probability matrix if and only if the diagonal elements are non-negative. (If the diagonal elements are non-negative, then the off-diagonal elements are bounded above by one.) It is easy to imagine cases where this is not satisfied. Consider, for example, a category with a very small stock of mass, but through which a large amount of mass is routed in a single time step (i.e., with the mass coming into the category largely balanced by mass leaving the category). In the modified microphysics that we are using, no more mass leaves a category in a time step than is available in that category. Therefore, the diagonal elements of \mathbf{P} are bounded by 0 and 1. For a category j with zero mass, the ratio $\dot{\rho}_{ij} / \rho_j$ would be zero divided by zero, which is undefined. Since N_j should be zero in these cases, it does not matter what probability is assigned in these cases, so a value of zero has been used in equation (11). Having defined \mathbf{P} in equation (11) and its relationship to the evolution of \mathbf{N} in equation (10), we can then use \mathbf{P} to move particles between categories in a stochastic way that captures the underlying Eulerian statistics without generating fractional particles.

c. Initial conditions and outline of a timestep

In practice, N_p particles are randomly distributed in the domain with the constraint that N_i^* is statistically homogeneous in three-dimensional space with the same value for all i . This is achieved by computing the fraction of the domain-wide water mass M_{tot} that resides in each grid-box. This gives the probability for each particle to be initially seeded into a certain grid-box. The position of each particle within a grid-box is also chosen stochastically. Each particle can then be interpreted as representing a water mass of $\delta m = M_{tot}/N_p$. In a similar stochastic approach, the initial category is assigned to each particle with a probability distribution given by the fractions of total grid-box water mass explained by the individual categories. For example, the simulations presented below start from an atmosphere without condensate such that only vapor particles are seeded initially.

Once the initial conditions are set, the outline of a time step δt within the stochastic Lagrangian particle framework is as follows:

- 1) Given the parameterized mass-exchange rates $\dot{\rho}_{ij}(t)$ and the mass distributions $\rho_j(t)$ in a grid box of the Eulerian host model, obtain the probability matrix $\mathbf{P}(t)$ from equation (11).
- 2) For each particle in that grid box, use a random number generator to decide if, given the transition probabilities in $\mathbf{P}(t)$, the particle switches to another category or not.
- 3) Interpolate \mathbf{u}_a and \mathbf{u}_{if} to the particle's position and advance the particle from t to $t + \delta t$ using (2).

3. Large-eddy simulations

a. General description

Large-eddy simulations are carried out using Das Atmosphärische Modell (DAM, Romps 2008). DAM solves the compressible equations in flux form using a split-explicit (Klemp et al. 2007) total-variation-diminishing (TVD) 3rd-order Runge-Kutta (RK3) discretization in time (Shu and Osher 1988). Advection is discretized using a 3rd-order upstream scheme and a positive-definite flux limiter (Thuburn 1996) is applied to the moisture scalars. Following the concept of implicit LES (e.g., Margolin et al. 2006), no subgrid-scale (SGS) turbulence closure is applied. The lateral boundary conditions are cyclic. A no-slip bottom boundary condition with zero surface sensible and latent heat flux is applied.

The microphysical mass-exchange rates $\dot{\rho}_{ij}$ among six water classes are parameterized using an adapted Lin-Lord-Krueger one-moment bulk scheme (Lin et al. 1983; Lord et al. 1984; Krueger et al. 1995). The six water classes are water vapor, cloud liquid water, cloud ice, rain, snow, and graupel. The original version of this scheme contained several ad-hoc limiters for individual conversion processes. However, the mass-exchange rates $\dot{\rho}_{ij}$ were not scaled to avoid negative masses, which then had to be clipped after the microphysics call, followed by a mass-conserving rescaling of the resulting tendencies. Here, we remove the limiters of individual process rates and scale the final mass-exchange rates $\dot{\rho}_{ij}$ of each category j such that the total sink of a mass during one Euler step $\delta t \sum_{j \neq i} \dot{\rho}_{ij}$ does not exceed the available mass. Also, the evaporation of melting snow and graupel has been added to the scheme following Eq. (27) in Rutledge and Hobbs (1983), but applying coefficients consistent with the formulation by Lin et al. (1983) for melting (their Eqs. (32) and (47)).

Following Yeo and Romps (2013), the Eulerian fields are mapped onto the Lagrangian particles using a third-order WENO approximation (Shu 1998). The equation of particle motion (2) is integrated using TVD-RK3. Particles track the resolved flow and thus no SGS turbulent contributions are added to particle velocities (following, e.g., Boing et al. 2012; Yeo and Romps 2013). A “bounce-back” boundary condition is applied at $z = 0$ and $z = 20$ km. Only precipitating particles ($u_{if} \neq 0$) may penetrate through the lower boundary.

b. Simulation setup

Two simulations of warm and moist bubbles are presented in this paper, REF and MOIST, with the intention to mimic cumulus-congestus clouds. Bubbles have frequently been studied in numerical frameworks (e.g., Carpenter et al. 1998; Yeo and Romps 2013) due to existing and quasi-equivalent laboratory frameworks (e.g., Batchelor 1954) and due to the similarity to observed atmospheric convection (Scorer and Ludlam 1953; Blyth et al. 1988; Damiani et al. 2006). The bubble is initiated in the center of the domain into an otherwise horizontally homogeneous background atmosphere. The latter has been obtained as domain mean from a previous cloud-resolving simulation of an atmosphere in radiative-convective equilibrium (RCE) and thus represents a tropical atmosphere. A fixed sea surface temperature of 300 K and interactive shortwave and longwave radiation were used for this simulation (see Romps and Kuang 2011, section 3). The perturbation is prescribed by

$$T(r, z) = T_0(z) + (1 + \zeta) \exp \left[-(r/r_b)^2 - (z/z_b)^2 \right], \quad (12)$$

with $r = \sqrt{x^2 + y^2}$, height z , background temperature profile $T_0(z)$, $r_b = 1000$ m, $z_b = 500$ m, and random perturbations $\zeta \in [-0.1, 0.1]$.

The two simulations differ in their specified relative humidity profiles. In simulation REF, the water vapor mixing ratios are adapted to the perturbed temperature to obtain the original relative humidity distribution of the RCE profile. In simulation MOIST, the relative humidity is set by

$$RH_{\text{MOIST}} = 0.25 + 0.75RH_{\text{REF}}, \quad (13)$$

which reduces the saturation deficit in MOIST by 25% in each grid-box. In both simulations, the initial density is then specified to give hydrostatic balance in each grid column. MOIST results in a deeper convective cloud and more intense rainfall than REF. As in Yeo and Romps (2013), a domain size of $20 \times 20 \times 27.5$ km³ and a grid-spacing of 50 m has been chosen. Depending on the local CFL condition, the timestep switches between 1 and 2 s. Simulations end after $\Delta t = 120$ min and capture the complete life cycle of the convective clouds. Simulations are initialized with $N_p = 4 \cdot 10^7$ particles, corresponding to an equivalent average water mass per particle δm of 513 kg and 535 kg for REF and MOIST, respectively.

Note that two additional sensitivity experiments, REF_MAR and MOIST_HAIL, have been carried out to address the sensitivity of our main findings to selected microphysical properties of the clouds. These experiments are described in the appendix.

c. Comparison of Eulerian and Lagrangian statistics

Time series of rain rates have been obtained from both the Eulerian sedimentation fluxes and from counting Lagrangian particles permeating the surface (Fig. 1a). The agreement between Eulerian and Lagrangian rain rates is excellent, indicating that the temporal evolution of microphysics and transport is well represented by the stochastic Lagrangian particle framework. The difference between the total Eulerian and Lagrangian rainfall is only 4% for both REF and MOIST, with the Lagrangian rain yield the larger of the two. Figure 1b illustrates the sensitivity of the obtained statistics to the number of seeded particles in simulation MOIST. The Lagrangian statistics converge already at $N_p < 4 \cdot 10^7$. Differences begin to show up in rainfall statistics if every 4th particle is sampled. Sampling only every 128th particle (i.e., $N_p \approx 3 \cdot 10^5$) results in considerable fluctuations of the surface rainfall rate.

Further evidence for the excellent performance of the new framework is given by Fig. 2, which shows horizontally averaged particle number densities (dashed) and Eulerian mass densities (solid) for the different hydrometeor species after 24 min of simulation MOIST. The bottom axis is scaled such that overlying curves would indicate a statistically homogeneous vertical profile of N_i^* . Besides small statistical fluctuations of the ice and snow-particle profiles (note the factor 10 scaling) and a slight overrepresentation of rain mass at low levels, the Eulerian hydrometeor distributions

are very well captured by the respective particle categories. Analogous results are obtained for horizontal distributions. The remaining overestimation of the total rainfall ($\sim 4\%$) by Lagrangian statistics for $N_p = 4 \cdot 10^7$ is due to the numerical diffusion of the Eulerian solver. One-dimensional advection tests revealed that mass is diffused out of a shock-like falling perturbation in hydrometeor mass. This effectively leads to a slight increase of N^* (decrease of Eulerian mass) for the rain category. The small deviations for rain at lower levels reflect this behavior of the Eulerian solver.

4. Water transport by cumulus clouds

a. Transilient matrix for water

Transilient matrices have proven useful in studies of the convective transport by large eddies (Stull 1984; Romps and Kuang 2011). In contrast to the eddy-diffusivity theory for local turbulence, they describe the turbulent mass flux between points separated in space. An element $b(z, z_o)$ in such a matrix quantifies the non-local mass flux ($\text{kg m}^{-2} \text{s}^{-1}$) from within a layer of unit depth centered around z_o to a layer of unit depth centered around z . Thus, a transilient matrix has units $\text{kg m}^{-4} \text{s}^{-1}$. Using the described particle framework, the transilient matrix for dry air is extended here to water mass. The flux described by this matrix will include water transport from hydrometeor free fall and thus also include fluxes across the surface. Since the particles' history is known, the flux in such a matrix may also be subsetted to water mass that satisfies certain conditions (e.g., particular transitions between water categories).

Within this Lagrangian particle framework, the transilient flux $b(z, z_o)$ from within a layer of depth δz centered around z_o to a layer of depth δz centered around z is defined by

$$b(z, z_o) = \frac{\delta m}{A \delta z^2 \Delta t} \sum_{k=1}^{N_p} \mathcal{A}_k \mathcal{I}_z[z_k(t = \Delta t)] \mathcal{I}_{z_o}[z_k(t = 0)]. \quad (14)$$

Here, $\mathcal{I}_z[z_k]$ is a binary indicator that returns one if $z_k \in [z - \delta z/2, z + \delta z/2]$ and zero otherwise, and similarly for $\mathcal{I}_{z_o}[z_k]$. To include the flux of water across the surface, one additional row is added to the matrix and all particles with $z(t = \Delta t) = 0$ are added to this additional destination layer of arbitrary thickness. For illustration purposes we chose a layer of thickness δz centered around $-\delta z/2$. Fluxes are averaged over the whole domain area A and over the simulation period Δt . The binary activity operator \mathcal{A}_k , which takes values of zero or one, subsets the particles to those that satisfy a certain condition during period Δt . If particle k entrains into the cloud at least once during the simulation (i.e., the sum of the Eulerian cloud-liquid and cloud-ice mass fractions at the location of the particle exceeds $10^{-5} \text{ kg kg}^{-1}$ at some point in its history), then $\mathcal{A}_k^{\text{ent}} = 1$; otherwise, $\mathcal{A}_k^{\text{ent}} = 0$. If particle k condenses at least once (i.e., enters any of the non-precipitating or precipitating cloud-condensate categories), then $\mathcal{A}_k^{\text{con}} = 1$; otherwise, $\mathcal{A}_k^{\text{con}} = 0$. If the particle enters a precipitating hydrometeor at least once (i.e., enters the rain, snow, or graupel category), then $\mathcal{A}_k^{\text{prec}} = 1$; otherwise, $\mathcal{A}_k^{\text{prec}} = 0$. For each of these three activity operators, there is a corresponding transilient matrix, which is given by equation (14) with the labels “ent”, “con”, or “prec” on both \mathcal{A}_k and b . By definition, $\mathcal{A}_k^{\text{ent}} \geq \mathcal{A}_k^{\text{con}} \geq \mathcal{A}_k^{\text{prec}}$, so it follows immediately that $b^{\text{ent}} \geq b^{\text{con}} \geq b^{\text{prec}}$.

Fig. 3 shows the log base 10 of b^{ent} and b^{con} for both simulations. A layer thickness of $\delta z = 50 \text{ m}$ has been used to construct these plots and the lowest row centered at $-\delta z/2$ has been stretched for a better visualization of surface rainfall. The horizontal and vertical axes show origin heights z_o and destination heights z , respectively. In general, the area above the diagonal indicates water mass that experienced a net lifting, whereas areas below the diagonal show water that ends up at levels below its origin. Note that the difference between b^{ent} and b^{con} equals the transilient matrix of vapor that entrains, but never condenses.

The transilient matrix for entrained water b^{ent} (Figs. 3a,b) shows significant fluxes along and right below the diagonal, corresponding to water vapor that ends up where it started or somewhat below. Since the matrix for water includes hydrometeor free fall, diagonal elements do not necessarily correspond to small local eddies. However, since the heavily populated elements around the diagonal are missing in the matrix for condensed water b^{con} (Figs. 3c,d), local entrainment and detrainment of vapor indeed explains the relatively large population of diagonal (and right-below diagonal) elements in b^{ent} . Disentangling the individual displacements due to upward and downward motion of dry air and due to free fall showed that the large population right below the diagonal is indeed caused nearly exclusively by downward motion in unsaturated regions, rather than by hydrometeor free fall. On average, the net upward displacement of water mass for these highly-populated elements below the diagonal is about 500 m, the net downward displacement however about 1500 m. The matrix elements more than ~ 1 -km below the diagonal result almost exclusively from hydrometeor free fall. The below-surface row in the matrices indicates that layers below 400 m contribute more to surface rainfall than layers of comparable thickness higher up. However, contributions to surface rainfall also originate from levels almost as high as the cloud top.

A strong net upwards flux of water can be seen mostly for origin levels below 400 m in b^{ent} (Figs. 3a,b), but also for origin levels above 1000 m. Significant water mass is lifted from within the bubble and effectively displaced to heights up to 7 and 10 km in REF and MOIST, respectively. Little water entrains at levels right above the initial bubble (i.e., between 400 and 1000 m). As seen from b^{con} , only a fraction of the lifted water actually condensed (Figs. 3c,d). A caveat to such a comparison of b^{ent} and b^{con} is that some of the net upward flux of condensing water is water that is carried upwards, falls back down as precipitation, and evaporates above its original height. This contribution will be quantified below.

Recall that elements more than ~ 1 -km below the diagonal result from the evaporation of falling hydrometeors. As seen from b^{con} , a significant amount of precipitation evaporates and ends up at levels somewhat under the melting line, which is located at 4300 m. Further analysis showed that the increased flux to this specific level results from the evaporation of rain once significant snow and graupel has been melted. The melting of solid hydrometeors kicks in at the melting line, but becomes significant only further below due to a delay by relative humidity effects (see Lin et al. 1983, Eq. (32)).

The mass of water vapor entrained from a given height interval divided by the total mass of water vapor entrained from all heights is shown by the solid lines in Figs. 4a,b. We denote this “fraction of entrained vapor per height” by f_e , which has units of m^{-1} . In terms of the transilient matrix b^{ent} , f_e is given by

$$f_e(z_o) = \frac{\int_{-\delta z}^{\text{top}} dz b^{\text{ent}}(z, z_o)}{\int_{-\delta z}^{\text{top}} dz \int_0^{\text{top}} dz_o b^{\text{ent}}(z, z_o)}. \quad (15)$$

In Figs. 4a,b, the dashed curves show the mass of water vapor that is rained out from a given height interval, divided by the total rainfall. We denote this here by f_r with units of m^{-1} . In terms of the transilient matrix b^{ent} , f_r is given by

$$f_r(z_o) = \frac{\int_{-\delta z}^0 dz b^{\text{ent}}(z, z_o)}{\int_{-\delta z}^0 dz \int_0^{\text{top}} dz_o b^{\text{ent}}(z, z_o)}, \quad (16)$$

whereby integral $\int_{-\delta z}^0 dz$ denotes flux across the surface. Both f_e and f_r are largest for the lowest 400 m, show a minimum right above, and reveal further contributions from higher up. To obtain the integral fraction of vapor originating from below cloud base ($z_b = 400$ m) and the related rainfall fraction, we further quantify $F_e^{<B} = \int_0^{z_b} dz' f_e(z')$ and $F_r^{<B} = \int_0^{z_b} dz' f_r(z')$. The former evaluates to 0.31 and 0.28 and the latter to 0.61 and 0.51 for REF and MOIST, respectively. In

other words, only about one third of all vapor that entrains into the cloud is provided through the cloud base. However, this contribution makes up for 50% or even more of the total surface rainfall. Very similar numbers are obtained for congestus clouds with modified microphysical properties (see appendix). Apparently, vapor entrained through cloud base is more efficiently converted into rainfall (i.e., has a higher drying ratio) than vapor entrained laterally. Considering these results, the difference between the two simulated clouds seems fairly small. The fraction of rain from above cloud-base is somewhat higher in MOIST, since the fractional entrainment $F_e^{>B} = 1 - F_e^{<B}$ is larger and since – as will be shown below – the relative difference in condensation efficiencies between REF and MOIST is largest for vapor that entrains into the upper parts of the cloud where the updraft is enhanced in MOIST.

b. Cloud efficiencies

The efficiencies of two different water entrainment pathways, through cloud base and laterally, are analyzed in this section in more detail. With the help of the transilient matrices b^{ent} , b^{con} , and b^{prec} (the latter is not shown), the efficiencies for water originating from in between heights z_1 and z_2 can be defined as

$$\text{DR}(z_1, z_2) = \frac{\int_{-\delta z}^0 dz'' \int_{z_1}^{z_2} dz' b^{\text{prec}}(z'', z')}{\int_{-\delta z}^{\text{top}} dz'' \int_{z_1}^{z_2} dz' b^{\text{ent}}(z'', z')} \quad (17)$$

$$\text{CE}(z_1, z_2) = \frac{\int_{-\delta z}^{\text{top}} dz'' \int_{z_1}^{z_2} dz' b^{\text{con}}(z'', z')}{\int_{-\delta z}^{\text{top}} dz'' \int_{z_1}^{z_2} dz' b^{\text{ent}}(z'', z')} \quad (18)$$

$$\text{FE}(z_1, z_2) = \frac{\int_{-\delta z}^{\text{top}} dz'' \int_{z_1}^{z_2} dz' b^{\text{prec}}(z'', z')}{\int_{-\delta z}^{\text{top}} dz'' \int_{z_1}^{z_2} dz' b^{\text{con}}(z'', z')} \quad (19)$$

$$\text{SE}(z_1, z_2) = \frac{\int_{-\delta z}^0 dz'' \int_{z_1}^{z_2} dz' b^{\text{prec}}(z'', z')}{\int_{-\delta z}^{\text{top}} dz'' \int_{z_1}^{z_2} dz' b^{\text{prec}}(z'', z')}, \quad (20)$$

such that, e.g., efficiencies for vapor from below cloud base are obtained for $z_1 = 0$ and $z_2 = z_b$. Again, note that $\text{DR} = \text{CE} \cdot \text{PE}$ with $\text{PE} = \text{FE} \cdot \text{SE}$. Note that these height-resolved efficiencies cannot be calculated without the aid of the Lagrangian framework.

Table 1 lists the efficiencies obtained for the entirety of the cloud, for vapor originating below cloud base, and for vapor originating from above cloud base. The emerging picture of the water processing by each of the two pathways is illustrated in Fig. 5. The red pathway corresponds to vapor entrained through cloud base and the blue pathway corresponds to vapor entrained laterally. Of the total water that entrained into the cloud at least once, the numbers are the percentages that participate at least once in each process. For example, in the REF simulation, 31% of the vapor that enters the cloud does so through the cloud base. Of that 31%, 11% condenses and 20% gets detrained from the cloud without ever condensing. Of that 11% that condenses, 7% becomes precipitation, while 4% is detrained by the cloud before forming precipitation. Of the 7% that precipitates, 5% survives all the way down to the surface, while the other 2% evaporates into clear air: 1.6% above cloud base and 0.4% below cloud base. The fraction of precipitation that evaporates above cloud base is significant: $1.6\%/7\% = 23\%$. For example, this is larger than the upper limit of 15% chosen for the fraction of precipitation evaporating above cloud base in the buoyancy-sorting model of Emanuel (1981). However, it is also possible that the fraction of evaporated rain is somewhat too large in our model due to the use of a one-moment parameterization (Bryan and Morrison 2011).

The overall DR of the cloud results from the linear combination of the DRs of the two pathways with weights corresponding to the respective entrainment fraction. More than two thirds of the

vapor is entrained laterally, but with a very low DR. The vapor entrained through cloud base indeed has a larger DR, but its contribution to the overall entrainment is considerably smaller. As a consequence, the overall DR is only about half that of the DR for vapor entrained through the cloud base. Thus, the cloud's ability to convert vapor to surface rainfall is highly constrained by inefficient laterally entraining vapor. Both the fraction of vapor that condenses (CE) and the fraction of condensate that reaches the ground (PE) are smaller for water entraining laterally than for water entraining through cloud base.

Although REF and MOIST are similar in many regards, there are some important differences, too. The DR of laterally entraining vapor in MOIST is twice as large as in REF, and the overall DR is 50% larger. This is a consequence of both larger CE and larger PE. Most likely, the enhancement of CE in MOIST results from both a reduced dry-air dilution of the cloud and from a larger contribution from ice-phase microphysics (due to the MOIST cloud reaching 3 km higher than the REF cloud). This is reflected also in larger FEs. Note, however, that the deeper cloud in MOIST implies smaller SEs due to the formation of precipitation at higher altitudes and due to the smaller fall speeds of ice-crystals. Both factors increase the time it takes for a precipitation particle to reach the ground and thereby lower its chance to fall out. Nevertheless, the mean PE is larger in MOIST. Very similar efficiencies have been obtained from two sensitivity experiments with modified microphysics, as described in the appendix.

5. Dependence of efficiencies on height and time

To better understand the different processing of water by the two entrainment pathways, the dependence of efficiencies (17-20) on the vapor origin height is studied in more detail in this section. Figure 6 shows profiles of DR, CE, FE, and SE as obtained for z_1 ranging from 0 to 10 km in 50 m intervals and $z_2 = z_1 + 50$ m. The vertical axis corresponds to vapor origin levels such that multiplication of CE, FE, and SE yields DR. The precipitation efficiency PE, i.e., the product of FE and SE, is shown by the dashed black lines. DR has its largest values for vapor originating near the surface, very small values at 500 and 1000 m, and then monotonically decreasing values above an origin-level of 2 km. The vertical profile of DR is highly correlated with and highly constrained by the profile of CE. Only near the cloud top is DR controlled through SE approaching zero. Besides small fluctuations, FE and SE decrease monotonically with vapor origin height thus implying a decrease of PE with vapor origin height.

a. Condensation efficiency

As seen in Figure 6, it is the condensation efficiency that is most responsible for the small drying ratios in the lower troposphere. An important question, then, is what physics sets the profile of CE. A natural hypothesis is that the $CE(z)$ is set by the mean vertical distance that vapor from z is lofted. Let us thus define a mean vertical lifting height $h(z)$ for the fraction of water vapor that originates from within a layer around height z and entrains at least once during the simulation (as indicated by $\mathcal{A}_k^{\text{ent}}$). More specifically, the mean lifting height is diagnosed for the fraction of those vapor particles that has never been in any condensed category before, as

$$h(z) = \int_0^{\Delta t} dt' \frac{1}{\sum_{k=1}^{N_p} \mathcal{A}_k^{\text{ent}} \mathcal{A}_k^{\text{vap}}(t')} \sum_{k=1}^{N_p} w_k^c(t') \mathcal{A}_k^{\text{ent}} \mathcal{A}_k^{\text{vap}}(t') \quad (21)$$

with $\mathcal{A}_k^{\text{vap}}(t)$ an indicator that is one if particle k has not yet been in any condensed water category at time t , and otherwise zero. The denominator in (21) equals the size of the sample of vapor particles that entrain at least once during the simulation but have not yet condensed at time t' . The in-cloud vertical velocity $w_k^c(t)$ of a particle k equals its vertical velocity $w_k(t)$ if the sum of the

Eulerian cloud-liquid and cloud-ice mass fractions at the location of the particle exceeds $10^{-5} \text{ kg kg}^{-1}$ at time t . Otherwise, if the particle is detrained at time t , then $w_k^c(t)$ is zero.

Given the distance $h(z)$, we should be able to find an approximation for $\text{CE}(z)$ based on the initial profile of the saturation mixing ratio q_v^* . The fraction of water particles that originate from z and remains in the vapor phase all the way up to $z + h(z)$ should be approximately equal to the ratio of $q_v^*(z + h(z))$ to $q_v^*(z)$. Therefore, the condensed fraction $\text{CE}(z)$ should be

$$\text{CE}(z) \approx 1 - \frac{q_v^*(z + h(z))}{q_v^*(z)}. \quad (22)$$

Figure 7a plots the actual profile of CE as the solid curve and the approximation of equation (22) as the dashed curve for both simulations. The mean vertical displacement $h(z)$ is shown in Fig. 7b. The agreement with the actual CE shows that the crucial parameter for CE is, indeed, the average distance lifted within saturated updrafts. Clearly, near-surface air is lifted up highest, while vapor entrained into the upper parts of the cloud is lifted least. The differences between the q_v^* profile of the environment (used in this calculation) and the q_v^* profile a parcel actually experiences within the cloud seem to be small and secondary to the profiles of CE. This is in line with the picture of a highly diluted cloud with little buoyancy (Zipser 2003; Romps and Kuang 2010; Muller et al. 2011; Singh and O’Gorman 2013).

Additional analysis revealed that most of the condensing particles that first entrain through cloud base are lifted in a very buoyant initial convective pulse and never detrain before condensing. Non-condensing vapor particles that originate from below cloud base are mostly entrained after this first pulse and rise within less buoyant sections of the cloud. The complex behavior of $h(z)$ between 0.5 and 1.5 km results from the vortex dynamics during the early stage of the rising bubble, as will be explained further below.

b. Vortex dynamics, detrainment, and re-entrainment

To explain the undulations in $h(z)$ (and, therefore, CE) below 1.5 km, we must consider the vortical structure of the initiating bubble. Figure 8 shows mean particle trajectories originating from within the bubble and its nearby surroundings. Water vapor sitting on top of the bubble ($500 < z < 800 \text{ m}$) is pushed to the sides by the rising bubble approaching from below and, in contrast to the convergent flow near the surface, the emerging divergent flow leads to significantly less entraining trajectories. This explains the gap in the entrainment profiles seen earlier from the profile of f_e and the transilient matrices (Figs. 3 and 4).

A vortex ring at $\sim 900 \text{ m}$ forms an exception to this divergent and detraining flow. Vapor is re-entrained into the wake of the thermal that passes on its way from below. The recycling occurs after about 11 min in REF (somewhat earlier in MOIST) when some of the parcels from below have just passed. The vortex ring is clearly seen also in the Eulerian cloud liquid water distribution, as it forms a downward leaping saturated outflow from the cloud and an engulfment of unsaturated air right below. Very similar circulations around thermals have been observed in cumulus clouds (Blyth et al. 2005; Damiani et al. 2006). The underlying process of entrainment into the thermal’s wake seems in line with the concept of a shedding thermal (Blyth et al. 1988).

c. Precipitation efficiency

The overall precipitation efficiency PE for the REF (MOIST) simulation, defined as the product of formation efficiency FE and sedimentation efficiency SE, is 33% (38%). The profile of PE, which is given by the product of the red and green curves in Fig. 6, is shown by the dashed black lines in the same Figure. The precipitation efficiency is greatest for vapor entrained into the cloud near the surface. Precipitation efficiencies for that near-surface vapor are about 40% for the REF simulation and about 50% for the MOIST simulation. PE decreases monotonically with vapor origin height, primarily due to a decrease of the sedimentation efficiency SE towards zero for

vapor entrained at the top of the cloud. Precipitation that forms in the upper parts of the cloud will have to survive the free fall over a larger distance to reach the ground. The decrease of FE with vapor origin height most likely reflects the liquid-water dependence of the growth by collision and coalescence. Vapor originating at low levels with high CE will produce more condensate and thus might favor a faster warm-rain formation than water entraining higher up with lower CE. Using similar arguments, the particle growth from the collision of solid and liquid hydrometeors is expected to decrease with origin height.

d. Time series

As discussed in the introduction, previous studies have attempted to define time series of drying ratios and precipitation efficiencies using Eulerian statistics. To see how these Eulerian statistics can be misleading, Figure 9a shows vapor entrainment rates and surface precipitation rates for MOIST. Average rates are computed for one-minute time intervals by counting entrainment events of vapor particles and rain-out events of rain particles. The standard approach is to define DR as the ratio of the instantaneous surface rainfall rate and vapor entrainment rate (blue curves). Time series analysis of such ratios have frequently been used to study efficiencies during different stages of convective storms (e.g., Ferrier et al. 1996; Cohen and McCaul 2007; Khain et al. 2008). However, DRs estimated as the ratio of instantaneous rates entail two issues. First, an obvious time lag between entrainment and rainfall exists. Second, instantaneous entrainment rates include water molecules that already entrained previously, thereby biasing the efficiency low. This second issue also affects the ratios of time-integrated totals.

The Lagrangian approach fixes both of these issues. Rain rates can be shifted and plotted as a function of the first entrainment time and entrainment rates can be obtained considering only first entrainment events (red curves in Fig. 9a). The entrainment rate calculated from first-entrainment events only is significantly smaller than the total entrainment rate, echoing a similar result for dry air (Yeo and Roms 2013). Figure 9b shows DR calculated in two different ways: the standard Eulerian way (blue curve) and new the Lagrangian way (red curve). The DR calculated using the Eulerian time series has a bimodal time series with maxima near the middle and end of the cloud's life cycle. In contrast, the DR calculated using the Lagrangian time series leads to a physically plausible result: the drying ratio reaches around 30% during the first 10 min and then tapers off to zero well before the cloud has dissipated. The fact that DR decreases in time as the cloud grows is in qualitative agreement with the profile of DR in Fig. 6b, which decreases monotonically with height above about 1.5 km.

Figures 9c,d illustrates the analogous concept for PE. Note that the standard precipitation time series $RR(\text{time})$ exceeds the condensation rate for times beyond 45 minutes (Fig. 9c). This is due to the lag between condensation and surface precipitation. On the other hand, the error made from counting condensation multiple times is small (i.e., the $COND_{\text{first}}$ and $COND_{\text{all}}$ curves are nearly identical). Figure 9d shows PE calculated in both the standard Eulerian fashion and with the new Lagrangian method. With the standard method, the precipitation efficiency ranges wildly between 0% and 1000%. With the new Lagrangian method, the precipitation efficiency starts at about 70%, dips down to 45%, rises to a second maximum of about 60% after 12 min, and then decreases smoothly to zero. If we picture the cloud rising with time, this agrees qualitatively with the PE profile in Fig. 6b, which shows PE decreasing with height.

6. Summary and conclusions

A stochastic Lagrangian particle framework has been developed here to track representative water molecules in large-eddy simulations of atmospheric convection. The framework allows for the tracking of molecules through both physical and microphysical space, providing a detailed view of how clouds process water. This makes it possible to track surface rainfall back to its original height and to study precipitation efficiency – and other efficiencies of water conversion –

as a function of the original height of water vapor. Simulations are carried out for two cumulus-congestus clouds rising through environments of different relative humidity.

In the first step of the analysis, the Lagrangian particle trajectories are used to calculate various transilient matrices for water. These transilient matrices differ from previous transilient matrices (e.g., Stull 1984; Romps and Kuang 2011) in the sense that they quantify the transport of water molecules instead of nitrogen molecules. Unlike nitrogen molecules, water molecules can move relative to the dry air (due to the free-fall speeds of precipitating hydrometeors) and there are sources and sinks of water molecules at the surface (due to surface vapor fluxes and surface precipitation).

In the second step, the transilient matrices are used to define and study the drying ratio DR of vapor molecules entrained at a specific height (i.e., the fraction of those molecules that reach the ground as precipitation). The drying ratio can be written as the product of the condensation efficiency CE and the precipitation efficiency PE. In turn, PE can be written as the product of a formation efficiency FE (i.e., efficiency of forming precipitation) and a sedimentation efficiency SE (i.e., efficiency of sedimenting to the surface), yielding $DR = CE \cdot FE \cdot SE$.

It is found here that boundary-layer and free-tropospheric water vapor make comparable contributions to surface precipitation. Although boundary-layer vapor rains out much more efficiently (i.e., higher DR) than free-tropospheric vapor, the latter dominates the vapor that enters the cloud. The inefficient laterally entrained vapor from the free troposphere constrains the overall DR of the cloud to values that are only half the DR of vapor from the boundary layer. As expected, lateral mixing reduces the overall drying ratio of the cloud.

The drying ratio DR of a cumulus congestus is most constrained by CE in the sense that, among the terms on the right-hand side of $DR = CE \cdot FE \cdot SE$, CE is the smallest and has the most vertical structure. It is shown here that $CE(z)$ (i.e., the condensation efficiency of water vapor from height z) can be approximated as $1 - q_v^*(z + h(z))/q_v^*(z)$, where $h(z)$ is the mean height that water vapor from z is lifted upwards in the cloud and q_v^* is the saturation vapor mixing ratio. The larger CE and DR of vapor originating from the boundary-layer results from its considerably larger vertical displacement $h(z)$. It remains to be clarified if ascent through a relatively protected cloud core is the process that favors the larger vertical displacement of boundary-layer vapor. The coherent involutions of the initial vortex ring formed by the rising bubble seem to support the concept for entrainment into the thermal's wake as proposed by Blyth et al. (1988).

The precipitation efficiency PE is found to be 33% and 38% for the dry and moist simulation, respectively. FE and SE have comparable values near the surface in the range of 60–80%. Both FE and SE decrease with vapor origin height, but SE decreases much more rapidly, so it is identified as the dominant control on PE for water entraining into the upper parts of the clouds. Water vapor that entrains and condenses in the cloud at higher altitudes has a lower chance of reaching the ground as precipitation primarily because it has to survive a larger distance towards the surface.

Although the decrease of conversion efficiencies with vapor origin height seems to be a general feature of congestus clouds, the individual efficiencies obtained might depend on the specific environment studied (e.g., relative humidity, wind shear) and might also depend on the employed parameterizations. For example, the evolution of the individual clouds might be affected by the way subgrid-scale turbulence is modeled. However, one could argue that adding a subgrid-scale representation for turbulent diffusion will increase lateral mixing at the cloud-air interface which leads to more entrainment of vapor which in turn should impede cloud growth. Although condensation efficiencies might thus be somewhat lower, the obtained 2/3 fraction for entrainment of vapor above cloud-base might then not be much affected. Sensitivity experiments for which selected microphysical properties had been modified revealed little sensitivity of the individual efficiencies and confirmed our main conclusions (see appendix). A different microphysics parameterization (e.g., two-moment instead of one-moment) might nevertheless yield somewhat different efficiencies. It is beyond the scope of this paper to test this sensitivity. A more general picture of cloud efficiencies should be pursued in future studies. An extension of this framework to a more realistic scenario, e.g., one with multiple clouds (shallow and deep cumulus) at a time, could provide a

more universal view on cloud efficiencies. Such an extension would then also have to deal with the issue that water molecules might reside within more than one cloud before they fall out.

Acknowledgments. This work was supported by the U.S. Department of Energy’s Atmospheric System Research, an Office of Science, Office of Biological and Environmental Research program, and by the Scientific Discovery through Advanced Computing (SciDAC) program funded by U.S. Department of Energy Office of Advanced Scientific Computing Research and Office of Biological and Environmental Research, under Contract No. DE-AC02-05CH11231. This research used computing resources of the National Energy Research Scientific Computing Center (NERSC), which is supported by the Office of Science of the U.S. Department of Energy under Contract DE-AC02-05CH11231, and computing resources of the Extreme Science and Engineering Discovery Environment (XSEDE), which is supported by National Science Foundation Grant OCI-1053575. Three anonymous reviewers are acknowledged.

APPENDIX

(In)sensitivity to microphysics

Two sensitivity experiments are described here in order to illustrate the robustness of our main findings to selected microphysical specifications. Time series of surface precipitation rate obtained from the Lagrangian particles in the original and the sensitivity runs are shown in Fig. 6. To better understand the underlying microphysics we split the particles into two groups: particles that are never part of a frozen-water category (i.e., warm-phase) and particles that are at least once part of a frozen-water category (i.e., mixed-phase). The total precipitation (i.e., all particles that reach the ground) is shown by solid curves and mixed-phase precipitation is shown by dashed curves.

REF_MAR uses the same setup as REF, but a different cloud-drop concentration N_b and relative dispersion D_b within the Berry-type formulation of autoconversion (see Lin et al. 1983, Eq. 50). In order to represent a more maritime cloud type, N_b is decreased from 1000 cm^{-3} to 50 cm^{-3} and D_b is increased from 0.15 to 0.36 (e.g., ?). REF_MAR produces a congestus cloud with an earlier onset of warm-rain precipitation and with less vigorous mixed-phase precipitation (see Fig. 6a).

The second experiment, MOIST_HAIL, is the same as MOIST, but uses a smaller intercept parameter N_{0g} for the graupel/hail size distribution. We adjust the original value of $N_{0g} = 4 \cdot 10^6 \text{ m}^{-4}$ to Lord et al. (1984)’s value of $N_{0g} = 4 \cdot 10^4 \text{ m}^{-4}$. As described by Krueger et al. (1995), the modified spectrum with reduced N_{0g} is closer to that of hail (rather than graupel) and differences are expected mostly due to the increased hydrometeor fall speed. In agreement with Krueger et al. (1995)’s findings, MOIST_HAIL results in a more shallow cloud than MOIST and a smaller graupel and ice content in the upper parts of the cloud. Figure 6b shows the earlier onset of mixed-phase precipitation due to the faster fall speed of hail.

Despite these differences, the modified congestus clouds lead to the same conclusions as REF and MOIST. The integral fraction of vapor originating from below cloud base and the related rainfall fraction are $F_e^{<B} = 30\%$ and $F_r^{<B} = 63\%$ for REF_MAR and $F_e^{<B} = 29\%$ and $F_r^{<B} = 51\%$ for MOIST_HAIL. These values agree with those of REF ($F_e^{<B} = 31\%$ and $F_r^{<B} = 61\%$) and MOIST ($F_e^{<B} = 28\%$ and $F_r^{<B} = 51\%$), respectively. The efficiencies (DR, CE, FE, SE) of the modified clouds are also very similar to the original simulations (see Table 6). To better understand this insensitivity of the efficiencies, we computed PE for the warm-phase particles and the mixed-phase particles separately. In case of REF_MAR, the insensitivity results from an increased PE of the warm-rain process that is counteracted by a smaller PE of the mixed phase process. MOIST_HAIL has a slightly higher mixed-phase PE than MOIST, but differences are fairly small.

References

- Auer, A. H., and J. D. Marwitz, 1968: Estimates of Air and Moisture Flux into Hailstorms on the High Plains. *J. Appl. Meteorol.*, **7**, 196–198.
- Batchelor, G. K., 1954: Heat convection and buoyant effects in fluids. *Quart. J. Roy. Meteor. Soc.*, **80**, 339–358.
- Blyth, A. M., W. A. Cooper, and J. B. Jensen, 1988: A study of the source of entrained air in Montana cumuli. *J. Atmos. Sci.*, **45**, 3944–3964.
- Blyth, A. M., S. G. Lasher-Trapp, and W. A. Cooper, 2005: A study of thermals in cumulus clouds. *Quart. J. Roy. Meteor. Soc.*, **131**, 1171–1190.
- Boing, S. J., H. J. J. Jonker, A. P. Siebesma, and W. W. Grabowski, 2012: Influence of the Subcloud Layer on the Development of a Deep Convective Ensemble. *J. Atmos. Sci.*, **69**, 2682–2698.
- Braham, R. R., 1952: The water and energy budgets of the thunderstorm and their relation to thunderstorm development. *J. Meteorol.*, **9**, 227–242.
- Bryan, G. H., and H. Morrison, 2011: Sensitivity of a simulated squall line to horizontal resolution and parameterization of microphysics. *Mon. Wea. Rev.*, doi:10.1175/MWR-D-11-00046.1.
- Carpenter, R. L., Jr., K. K. Droegemeier, and A. M. Blyth, 1998: Entrainment and detrainment in numerically simulated cumulus congestus clouds. Part III: Parcel Analysis. *J. Atmos. Sci.*, **55**, 3440–3455.
- Cohen, C., and E. W. McCaul, Jr., 2007: Further results on the sensitivity of simulated storm precipitation efficiency to environmental temperature. *Mon. Wea. Rev.*, **135**, 1671–1684.
- Damiani, R., G. Vali, and S. Haimov, 2006: The structure of thermals in cumulus from airborne dual-doppler radar observations. *J. Atmos. Sci.*, **63**, 1432–1450.
- Emanuel, K. A., 1981: A similarity theory for unsaturated downdrafts within clouds. *J. Atmos. Sci.*, **38**, 1541–1557.
- Fankhauser, J. C., 1988: Estimates of thunderstorm precipitation efficiency from field-measurements in CCOPE. *Mon. Wea. Rev.*, **116**, 663–684.
- Ferrier, B. S., J. Simpson, and W. K. Tao, 1996: Factors responsible for precipitation efficiencies in midlatitude and tropical squall simulations. *Mon. Wea. Rev.*, **124**, 2100–2125.
- Heus, T., G. Van Dijk, H. J. J. Jonker, and H. E. A. Van den Akker, 2008: Mixing in shallow cumulus clouds studied by Lagrangian particle tracking. *J. Atmos. Sci.*, **65**, 2581–2597.
- Khain, A. P., N. BenMoshe, and A. Pokrovsky, 2008: Factors determining the impact of aerosols on surface precipitation from clouds: An attempt at classification. *J. Atmos. Sci.*, **65**, 1721–1748.
- Kirshbaum, D. J., and R. B. Smith, 2008: Temperature and moist-stability effects on midlatitude orographic precipitation. *Q. J. Royal. Meteor. Soc.*, **134**, 1183–1199.
- Klemp, J. B., W. C. Skamarock, and J. Dudhia, 2007: Conservative split-explicit time integration methods for the compressible nonhydrostatic equations. *Mon. Wea. Rev.*, **135**, 2897–2913.
- Knight, C. G., and Coauthors, 2007: Association of parameter, software, and hardware variation with large-scale behavior across 57,000 climate models. *P. Natl. Acad. Sci. USA*, **104**, 12 259–12 264.

- Krueger, S. K., Q. A. Fu, K. N. Liou, and H. N. S. Chin, 1995: Improvements of an ice-phase microphysics parameterization for use in numerical simulations of tropical convection. *J. Appl. Meteorol.*, **34**, 281–287.
- Kuang, Z., and C. S. Bretherton, 2006: A mass-flux scheme view of a high-resolution simulation of a transition from shallow to deep cumulus convection. *J. Atmos. Sci.*, **63**, 1895–1909.
- Lasher-Trapp, S. G., W. A. Cooper, and A. M. Blyth, 2005: Broadening of droplet size distributions from entrainment and mixing in a cumulus cloud. *Quart. J. Roy. Meteor. Soc.*, **131**, 195–220.
- Lin, Y.-L., D. F. Richard, and H. D. Orville, 1983: Bulk parametrization of the snow field in a cloud model. *J. Appl. Meteor.*, **22**, 1065–1092.
- Lord, S. J., H. E. Willoughby, and J. M. Piotrowicz, 1984: Role of a parameterized ice-phase microphysics in an axisymmetric, nonhydrostatic tropical cyclone model. *J. Atmos. Sci.*, **41**, 2836–2848.
- Margolin, L. G., W. J. Rider, and F. F. Grinstein, 2006: Modeling turbulent flow with implicit LES. *J. Turbul.*, **7**, 1–27.
- Muller, C., P. A. O’Gorman, and L. E. Back, 2011: Intensification of precipitation extremes with warming in a cloud-resolving model. *J. Climate*, **24**, 2784–2800.
- Murray, F. W., and L. R. Koenig, 1972: Numerical experiments on the relation between microphysics and dynamics in cumulus convection. *Mon. Wea. Rev.*, **100**, 717–732.
- O’Gorman, P. A., and C. J. Muller, 2010: How closely do changes in surface and column water vapor follow Clausius-Clapeyron scaling in climate change simulations? *Env. Res. Let.*, **5**.
- Pauluis, O., and I. M. Held, 2002: Entropy budget of an atmosphere in radiative-convective equilibrium. Part I: Maximum work and frictional dissipation. *J. Atmos. Sci.*, **59**, 125–139.
- Phillips, V. T. J., and Coauthors, 2005: Anvil glaciation in a deep cumulus updraught over Florida simulated with the Explicit Microphysics Model. I: Impact of various nucleation processes. *Q. J. Royal. Meteor. Soc.*, **131**, 2019–2046.
- Respondek, P. S., A. I. Flossmann, R. R. Alheit, and H. R. Pruppacher, 1995: A theoretical study of the wet removal of atmospheric pollutants. Part V: The uptake, redistribution, and deposition of $(\text{NH}_4)_2\text{SO}_4$ by a convective cloud containing ice. *J. Atmos. Sci.*, **52**, 2121–2132.
- Romps, D. M., 2008: The Dry-Entropy Budget of a Moist Atmosphere. *J. Atmos. Sci.*, **65**, 3779–3799.
- Romps, D. M., 2011: Response of Tropical Precipitation to Global Warming. *J. Atmos. Sci.*, **68**, 123–138.
- Romps, D. M., and Z. Kuang, 2010: Do Undiluted Convective Plumes Exist in the Upper Tropical Troposphere? *J. Atmos. Sci.*, **67** (2).
- Romps, D. M., and Z. Kuang, 2011: A Transilient Matrix for Moist Convection. *J. Atmos. Sci.*, **68**, 2009–2025.
- Rutledge, S. A., and P. V. Hobbs, 1983: The mesoscale and microscale structure and organization of clouds and precipitation in mid-latitude cyclones. VIII. A model for the seeder-feeder process in warm-frontal rainbands. *J. Atmos. Sci.*, **40**, 1185–1206.

- Sanderson, B. M., C. Piani, W. J. Ingram, D. A. Stone, and M. R. Allen, 2008: Towards constraining climate sensitivity by linear analysis of feedback patterns in thousands of perturbed-physics GCM simulations. *Climate Dyn.*, **30**, 175–190.
- Scorer, R. S., and F. H. Ludlam, 1953: Bubble theory of penetrative convection. *Quarterly J. Roy. Meteor. Soc.*, **79**, 94–&.
- Shu, C.-W., 1998: Essentially non-oscillatory and weighted essentially non-oscillatory schemes for hyperbolic conservation laws. *Advanced Numerical Approximation of Nonlinear Hyperbolic Equations*, A. Quarteroni, Ed., Lecture Notes in Mathematics, Vol. 1697, Springer, 325–432.
- Shu, C. W., and S. Osher, 1988: Efficient implementation of essentially non-oscillatory shock-capturing schemes. *J. Comput. Phys.*, **77**, 439–471.
- Singh, M. S., and P. A. O’Gorman, 2013: Influence of entrainment on the thermal stratification in simulations of radiative-convective equilibrium. *Geophys. Res. Lett.*, **40**, 4398–4403.
- Smith, R. B., Q. Jiang, M. G. Fearon, P. Tabary, M. Dorninger, J. Doyle, and R. Benoit, 2003: Orographic precipitation and air mass transformation: An Alpine example. *Quart. J. Roy. Meteor. Soc.*, **129**, 433–454.
- Stull, R. B., 1984: Transilient turbulence theory .1. The concept of eddy-mixing across finite distances. *J. Atmos. Sci.*, **41**, 3351–3367.
- Sui, C.-H., X. Li, and M.-J. Yang, 2007: On the definition of precipitation efficiency. *J. Atmos. Sci.*, **64**, 4506–4513.
- Sui, C. H., X. F. Li, M. J. Yang, and H. L. Huang, 2005: Estimation of oceanic precipitation efficiency in cloud models. *J. Atmos. Sci.*, **62**, 4358–4370.
- Thuburn, J., 1996: Multidimensional flux-limited advection schemes. *J. Comput. Phys.*, **123**, 74–83.
- van den Heever, S. C., G. L. Stephens, and N. B. Wood, 2011: Aerosol Indirect Effects on Tropical Convection Characteristics under Conditions of Radiative-Convective Equilibrium. *J. Atmos. Sci.*, **68**, 699–718.
- Weisman, M. L., and J. B. Klemp, 1982: The dependence of numerically simulated convective storms on vertical wind shear and buoyancy. *Mon. Wea. Rev.*, **110**, 504–520.
- Yang, B., Y. Qian, G. Lin, R. Leung, Y. Zhang, and Y. Zhang, 2012: Some issues in uncertainty quantification and parameter tuning: a case study of convective parameterization scheme in the WRF regional climate model. *Atmos. Phys. Chem.*, **12**, 2409–2427.
- Yang, B., and Coauthors, 2013: Uncertainty quantification and parameter tuning in the CAM5 Zhang-McFarlane convection scheme and impact of improved convection on the global circulation and climate. *J. Geophys. Res. Atmos.*, **118**, 395–415.
- Yeo, K., and D. M. Romps, 2013: Measurement of convective entrainment using lagrangian particles. *J. Atmos. Sci.*, **70**, 266–277.
- Zhao, M., and P. H. Austin, 2005: Life cycle of numerically simulated shallow cumulus clouds. Part II: Mixing dynamics. *J. Atmos. Sci.*, **62**, 1291–1310.
- Zipser, E. J., 2003: *Some Views On Hot Towers after 50 Years of Tropical Field Programs and Two Years of TRMM Data*, Vol. 29. Amer. Meteor. Soc., 49–58 pp.

LIST OF TABLES

Table 1. Drying ratio (DR), condensation (CE), formation (FE), sedimentation (SE), and precipitation (PE) efficiency for the two simulations REF and MOIST. Efficiencies are shown for the entirety of the cloud and for two different pathways: for vapor entrained through cloud base (<B) and for vapor entrained above cloud base (>B). See text for definitions of these efficiencies. 21

Table A1. Drying ratio (DR), condensation efficiency (CE), formation efficiency (FE), and sedimentation efficiency (SE) of simulations REF, REF_MAR, MOIST, and MOIST_HAIL. 22

TABLE 1. Drying ratio (DR), condensation (CE), formation (FE), sedimentation (SE), and precipitation (PE) efficiency for the two simulations REF and MOIST. Efficiencies are shown for the entirety of the cloud and for two different pathways: for vapor entrained through cloud base (<B) and for vapor entrained above cloud base (>B). See text for definitions of these efficiencies.

	DR = CE × PE			PE = FE × SE	
REF	.08	.23	.33	.54	.62
REF (<B)	.16	.35	.46	.64	.71
REF (>B)	.04	.17	.25	.50	.50
MOIST	.12	.32	.38	.69	.55
MOIST (<B)	.21	.43	.50	.75	.66
MOIST (>B)	.08	.28	.30	.65	.46

Table A1. Drying ratio (DR), condensation efficiency (CE), formation efficiency (FE), and sedimentation efficiency (SE) of simulations REF, REF_MAR, MOIST, and MOIST_HAIL.

	DR = CE × PE			PE = FE × SE	
REF	.08	.23	.33	.54	.62
REF_MAR	.08	.21	.36	.57	.64
MOIST	.12	.32	.38	.69	.55
MOIST_HAIL	.13	.32	.39	.68	.58

LIST OF FIGURES

- Fig. 1.** Time series of surface precipitation rates ($10^{-5} \text{ kg m}^{-2} \text{ s}^{-1}$) are shown for (a) the two simulations REF and MOIST. Both (solid) Lagrangian statistics and (dashed) Eulerian rainrates are shown. In (b) Lagrangian statistics are computed for MOIST using different particle sampling intervals (i.e., every 128th particle has been sampled for the green curve). 25
- Fig. 2.** Vertical profiles of horizontally averaged Eulerian mass densities (solid) and Lagrangian particle number densities (dashed) are shown for MOIST after 24 min. Distributions are based on layers with a depth of 50 m each and are shown for the five hydrometeor species. The bottom axis is scaled by particle mass such that overlying curves would indicate a perfect match between Eulerian mass and particle number. Ice and snow densities have been scaled by a factor 10. 26
- Fig. 3.** Transilient matrices for water in REF and MOIST as obtained from the Lagrangian particle trajectories. Log base 10 of the water mass flux ($\text{kg m}^{-4} \text{ s}^{-1}$) is shown for water that (a,b) entrained at least once b^{ent} and (c,d) condensed at least once b^{con} . Note that the additional row added for particles that reached the surface has been stretched. 27
- Fig. 4.** The fraction of (solid) total entrainment f_e (m^{-1}) and of (dashed) total surface rainfall f_r (m^{-1}) as function of vapor origin level z_o for a) REF and b) MOIST. The integrals over the curves equal the total vapor entrainment and total rainfall, respectively. 28
- Fig. 5.** Mass of water (in percent of total) cycled through the simulated cloud through various physical and microphysical pathways for the (a) REF and (b) MOIST simulations. The total mass of water entrained (at least once) into the cloud is $1.7 \cdot 10^8 \text{ kg}$ and $2.7 \cdot 10^8 \text{ kg}$ for the REF and MOIST simulations, respectively. These numbers are based on efficiencies shown in Table 1 for vapor entrained through the (red) cloud base ($<B$) and vapor entrained laterally (blue) above the cloud base ($>B$). For example, in the MOIST simulation, 28% of the water that passes through the cloud does so by entering through the cloud base. Of that 28%, 12% condenses and 16% detrains from the cloud before it has a chance to condense. 29
- Fig. 6.** Vertical profiles of drying ratio (DR; black solid), condensation efficiency (CE; blue), formation efficiency (FE; red), sedimentation efficiency (SE; green), and precipitation efficiency (PE; black dashed) for simulations (a) REF and (b) MOIST. Ordinates correspond to vapor origin heights z_o . Light colors indicate results with 95%-confidence intervals larger than 0.25. 30
- Fig. 7.** Vertical profiles of a) the condensation efficiencies CE (solid) and its approximate form Eq. (22) (dashed) and b) mean vapor displacement height $h(z)$ from simulations (black) REF and (gray) MOIST. Ordinates correspond to vapor origin heights. 31
- Fig. 8.** Average particle trajectories and elapsed time (colors) are shown for selected particle origins from a) REF and b) MOIST. Coordinates of mean trajectories are obtained by averaging radial distance and height over all particles originating from within the same 50 m wide ring around the bubble's center and from within the same 50 m deep layer. Only non-precipitating particles are considered. Isolines of radially averaged Eulerian cloud condensate ($q_c + q_i$) are shown at $10^{-5} \text{ kg kg}^{-1}$ after 6, 12, and 18 min. 32
- Fig. 9.** Comparison of time series of drying ratios DR and precipitation efficiencies PE obtained from the standard Eulerian approach and the Lagrangian framework. Shown in a) are the vapor entrainment (ENTR) and rain rates (RR) ($10^{-4} \text{ kg m}^{-2} \text{ s}^{-1}$) used to construct the two time series of drying ratios shown in b). The Eulerian (Lagrangian) DR in b) is based on the

ratio of the blue (red) curves shown in a). Analogously, c) shows the condensation (COND) and rain rates (RR) used to construct the precipitation efficiencies shown in d). Again, the Eulerian (Lagrangian) PE in d) is based on the ratio of the blue (red) curves shown in c). $\text{Time}_{\text{entr}}$ and $\text{Time}_{\text{cond}}$ are time of entrainment and condensation, respectively. 33

Fig. A1. Time series of surface precipitation rates ($10^{-5} \text{ kg m}^{-2} \text{ s}^{-1}$) are shown for (a) REF and REF_MAR and (b) MOIST and MOIST_HAIL. Both (solid) total precipitation and (dashed) mixed-phase precipitation are shown. The latter is obtained from only those precipitating particles that were within a frozen-water category at least once during the simulation. 34

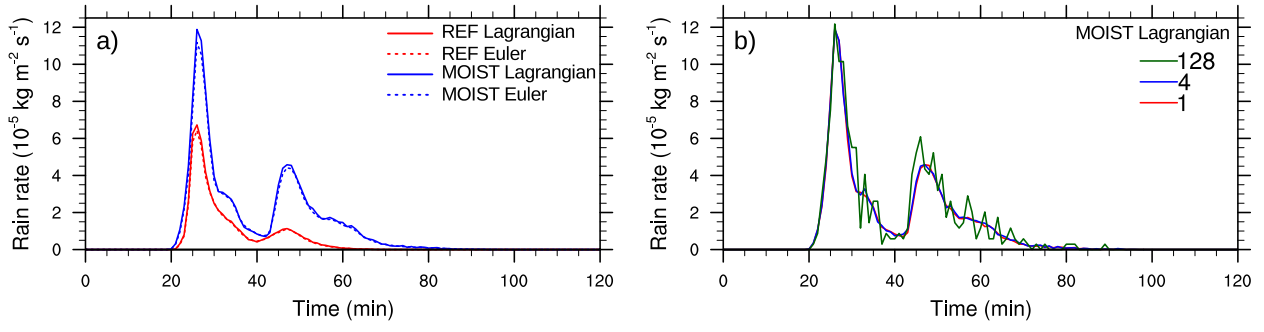


FIG. 1. Time series of surface precipitation rates ($10^{-5} \text{ kg m}^{-2} \text{ s}^{-1}$) are shown for (a) the two simulations REF and MOIST. Both (solid) Lagrangian statistics and (dashed) Eulerian rainrates are shown. In (b) Lagrangian statistics are computed for MOIST using different particle sampling intervals (i.e., every 128th particle has been sampled for the green curve).

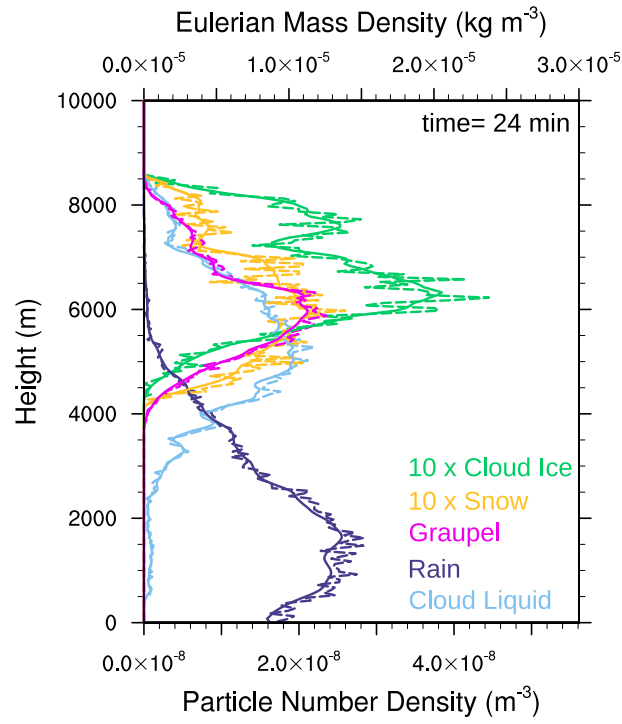


FIG. 2. Vertical profiles of horizontally averaged Eulerian mass densities (solid) and Lagrangian particle number densities (dashed) are shown for MOIST after 24 min. Distributions are based on layers with a depth of 50 m each and are shown for the five hydrometeor species. The bottom axis is scaled by particle mass such that overlying curves would indicate a perfect match between Eulerian mass and particle number. Ice and snow densities have been scaled by a factor 10.

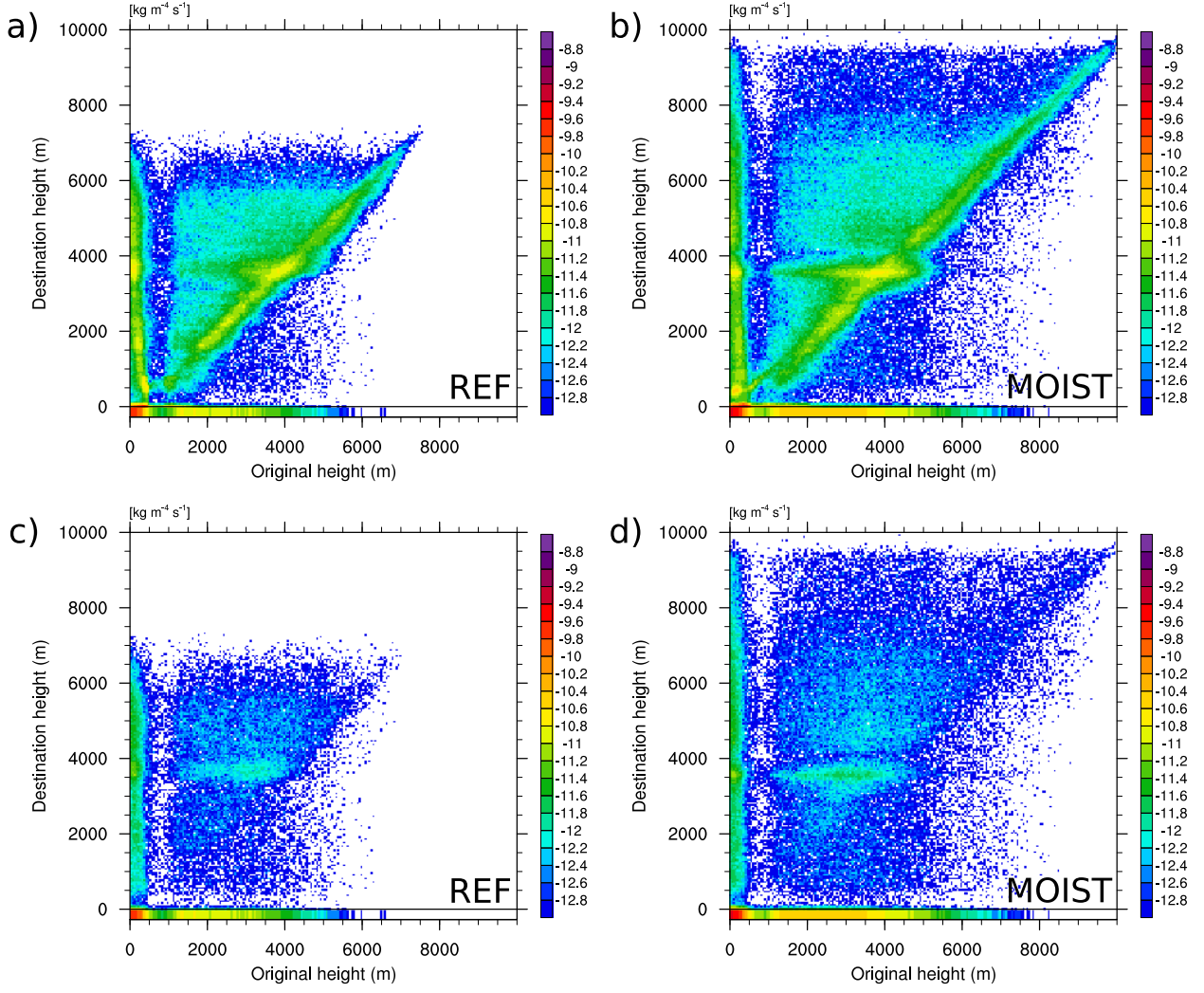


FIG. 3. Transilient matrices for water in REF and MOIST as obtained from the Lagrangian particle trajectories. Log base 10 of the water mass flux ($\text{kg m}^{-4} \text{s}^{-1}$) is shown for water that (a,b) entrained at least once b^{ent} and (c,d) condensed at least once b^{con} . Note that the additional row added for particles that reached the surface has been stretched.

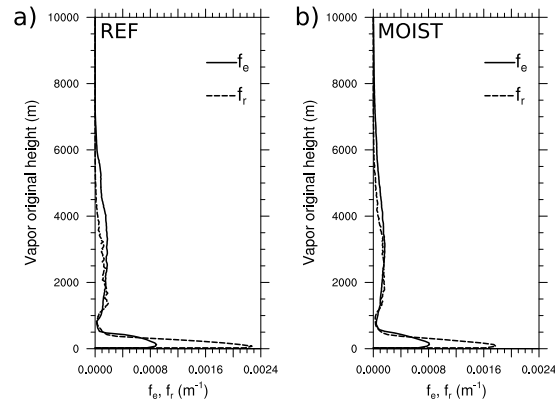


FIG. 4. The fraction of (solid) total entrainment $f_e \text{ (m}^{-1}\text{)}$ and of (dashed) total surface rainfall $f_r \text{ (m}^{-1}\text{)}$ as function of vapor origin level z_o for a) REF and b) MOIST. The integrals over the curves equal the total vapor entrainment and total rainfall, respectively.

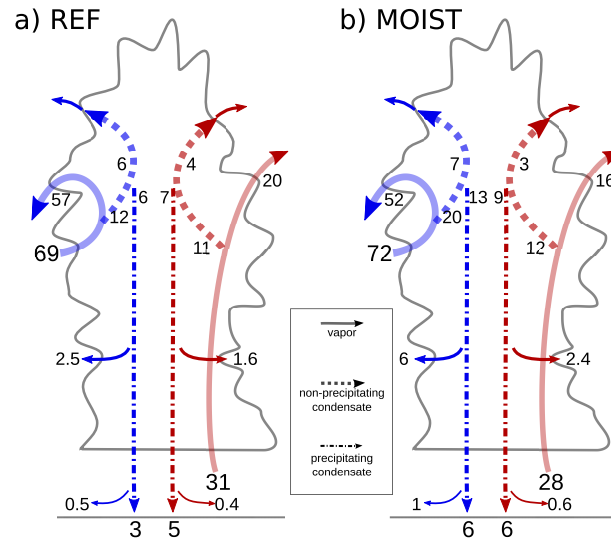


FIG. 5. Mass of water (in percent of total) cycled through the simulated cloud through various physical and microphysical pathways for the (a) REF and (b) MOIST simulations. The total mass of water entrained (at least once) into the cloud is $1.7 \cdot 10^8$ kg and $2.7 \cdot 10^8$ kg for the REF and MOIST simulations, respectively. These numbers are based on efficiencies shown in Table 1 for vapor entrained through the (red) cloud base (<B) and vapor entrained laterally (blue) above the cloud base (>B). For example, in the MOIST simulation, 28% of the water that passes through the cloud does so by entering through the cloud base. Of that 28%, 12% condenses and 16% detrains from the cloud before it has a chance to condense.

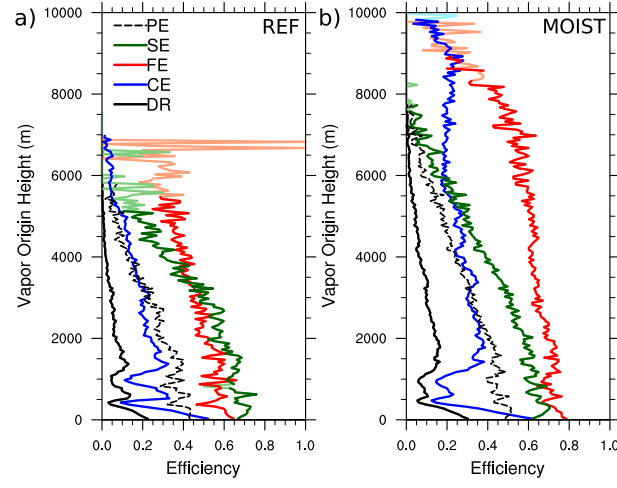


FIG. 6. Vertical profiles of drying ratio (DR; black solid), condensation efficiency (CE; blue), formation efficiency (FE; red), sedimentation efficiency (SE; green), and precipitation efficiency (PE; black dashed) for simulations (a) REF and (b) MOIST. Ordinates correspond to vapor origin heights z_o . Light colors indicate results with 95%-confidence intervals larger than 0.25.

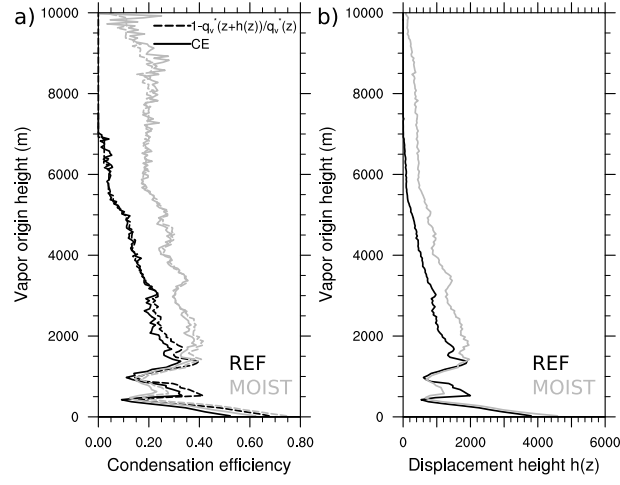


FIG. 7. Vertical profiles of a) the condensation efficiencies CE (solid) and its approximate form Eq. (22) (dashed) and b) mean vapor displacement height $h(z)$ from simulations (black) REF and (gray) MOIST. Ordinates correspond to vapor origin heights.

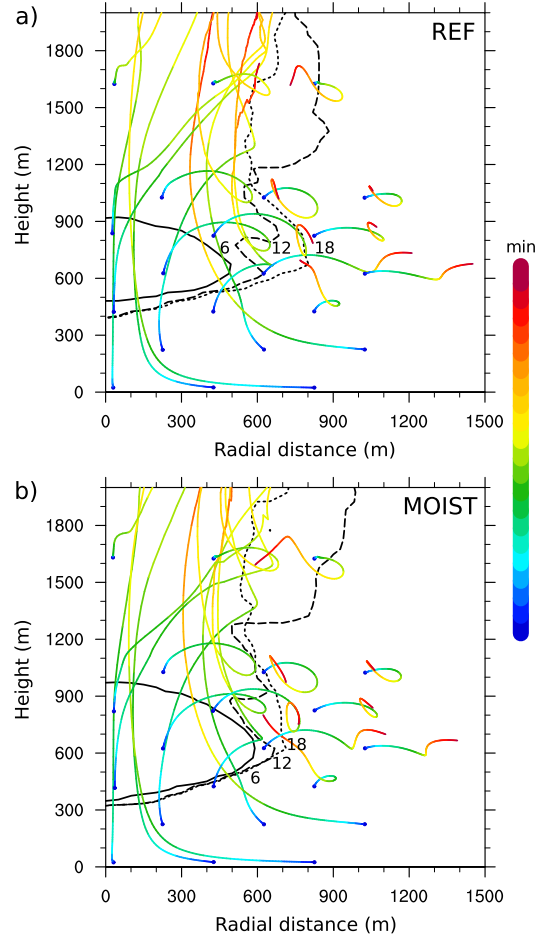


FIG. 8. Average particle trajectories and elapsed time (colors) are shown for selected particle origins from a) REF and b) MOIST. Coordinates of mean trajectories are obtained by averaging radial distance and height over all particles originating from within the same 50 m wide ring around the bubble's center and from within the same 50 m deep layer. Only non-precipitating particles are considered. Isolines of radially averaged Eulerian cloud condensate ($q_c + q_i$) are shown at $10^{-5} \text{ kg kg}^{-1}$ after 6, 12, and 18 min.

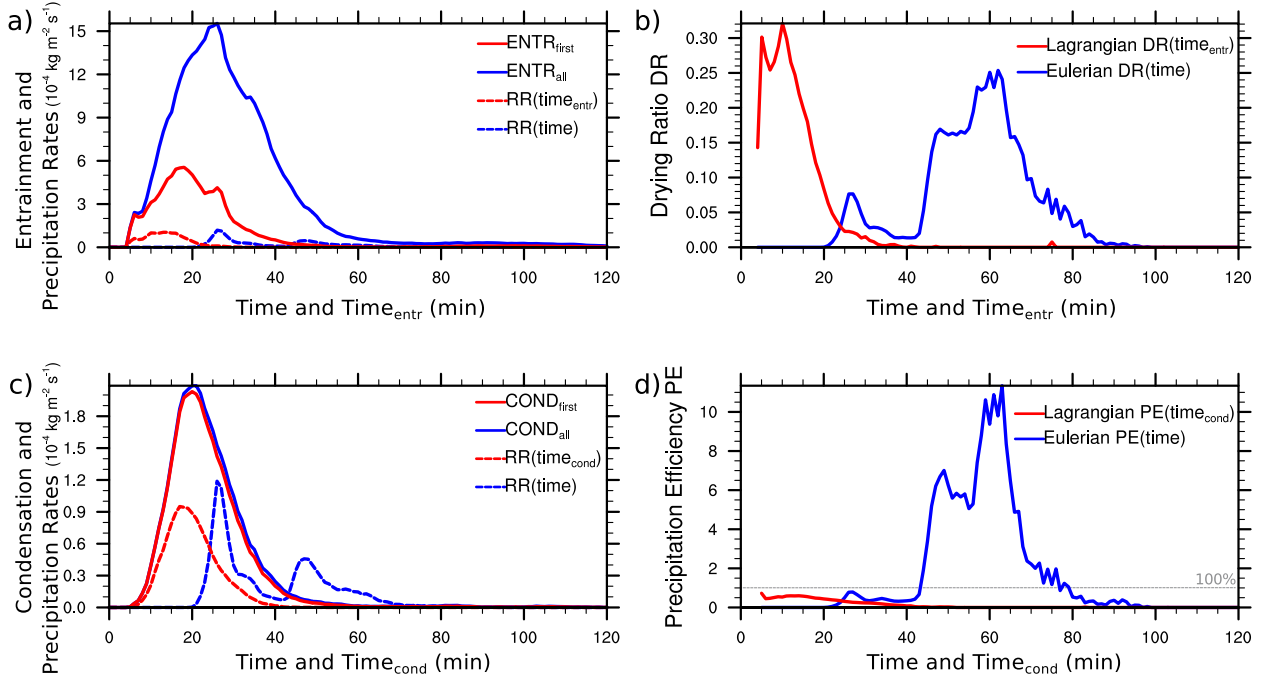


FIG. 9. Comparison of time series of drying ratios DR and precipitation efficiencies PE obtained from the standard Eulerian approach and the Lagrangian framework. Shown in a) are the vapor entrainment (ENTR) and rain rates (RR) ($10^{-4} \text{ kg m}^{-2} \text{ s}^{-1}$) used to construct the two time series of drying ratios shown in b). The Eulerian (Lagrangian) DR in b) is based on the ratio of the blue (red) curves shown in a). Analogously, c) shows the condensation (COND) and rain rates (RR) used to construct the precipitation efficiencies shown in d). Again, the Eulerian (Lagrangian) PE in d) is based on the ratio of the blue (red) curves shown in c). $\text{Time}_{\text{entr}}$ and $\text{Time}_{\text{cond}}$ are time of entrainment and condensation, respectively.

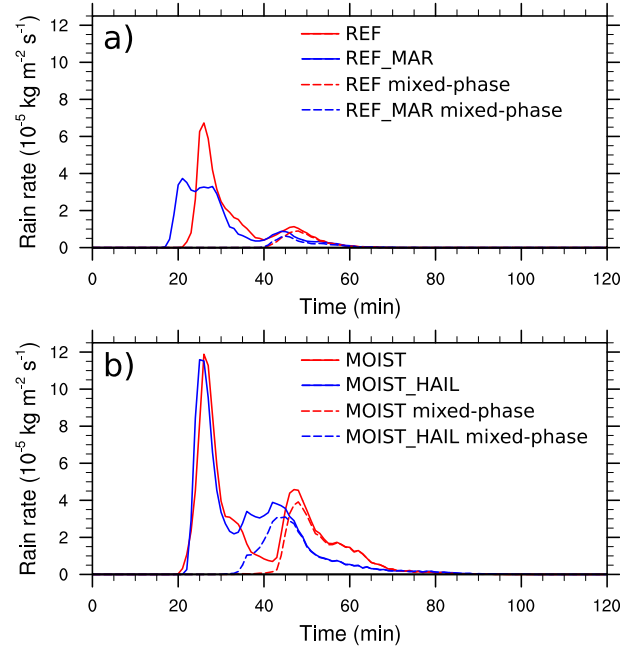


Fig. A1. Time series of surface precipitation rates ($10^{-5} \text{ kg m}^{-2} \text{ s}^{-1}$) are shown for (a) REF and REF_MAR and (b) MOIST and MOIST_HAIL. Both (solid) total precipitation and (dashed) mixed-phase precipitation are shown. The latter is obtained from only those precipitating particles that were within a frozen-water category at least once during the simulation.